Multi-objective and thermodynamic optimisation of a parabolic trough receiver with perforated plate inserts

Aggrey Mwesigye[1], Tunde Bello-Ochende[2,*], Josua P. Meyer[1]

[1]Department of Mechanical and Aeronautical Engineering, University of Pretoria
Private Bag X20, Hatfield 0028, South Africa
[2]Department of Mechanical Engineering, University of Cape Town
Private Bag X3, Rondebosch, 7701, South Africa

ABSTRACT

In this paper, multi-objective and thermodynamic optimisation procedures are used to investigate the performance of a parabolic trough receiver with perforated plate inserts. Three dimensionless perforated plate geometrical parameters considered in the optimisation include the dimensionless orientation angle, the dimensionless plate diameter and the plate spacing per unit meter. The Reynolds number varies in the range $1.02 \times 10^4 \leq \mathrm{Re} \leq 1.36 \times 10^6$ depending on the fluid temperature. The multi-objective optimisation was realised through the combined use of computational fluid dynamics, design of experiments, response surface methodology and the Non-dominated Sorted Genetic Algorithm-II. For thermodynamic optimisation, the entropy generation minimisation method was used to determine configurations with minimum entropy generation rates.

Keywords: Entropy generation minimisation, Heat transfer performance, Multi-objective optimisation, Parabolic trough receiver, Perforated plate inserts, Thermodynamic optimisation

NOMENCLATURE

A Area, m^2
A_a Collector's projected aperture area, m^2
a_c Collector aperture width, m
A_r Absorber tube's projected area, m^2
Be Bejan number
C_{2p} Inertial resistance factor, m^{-1}
c_p Specific heat capacity, $\mathrm{J\ kg^{-1}\ K^{-1}}$

---

* Corresponding author   Tel.: +27 21 650-3673; fax: +27 21 650-3240
                           E-mail address: tunde.bello-ochende@uct.ac.za, josua.meyer@up.ac.za

C_R	Concentration ratio
d	Perforated plate diameter, m
d_{gi}	Glass cover inner diameter, m
d_{go}	Glass cover outer diameter, m
d_{ri}	Absorber tube inner diameter, m
d_{ro}	Absorber tube outer diameter, m
DNI	Direct normal irradiance, Wm^{-2}
f	Darcy friction factor
h	Heat transfer coefficient, $\text{W m}^{-2}\text{K}^{-1}$
h_w	Wind heat transfer coefficient, $\text{W m}^{-2}\text{K}^{-1}$
I_b	Direct solar radiation. W m^{-2}
k	Turbulent kinetic energy per unit mass, $\text{m}^2\ \text{s}^{-2}$
L	Receiver length, m
Nu	Nusselt number
$N_{s,en}$	Entropy generation ratio = $S_{gen}/(S_{gen})_o$
P	Pressure, Pa
p	Perforated plate spacing, m
Pr	Prandtl number
q''	Heat flux, W m^{-2}
r	Radial position, m
Re	Reynolds number
S_{gen}	Entropy generation rate due to heat transfer and fluid friction, W K^{-1}
S'_{gen}	Entropy generation rate per unit meter $\text{W m}^{-1}\text{K}^{-1}$
$(S'_{gen})_H$	Entropy generation due to heat transfer per meter, $\text{W m}^{-1}\text{K}^{-1}$
$(S'_{gen})_F$	Entropy generation due to fluid friction per meter, $\text{W m}^{-1}\ \text{K}^{-1}$
S_m	Momentum source term
T	Temperature, K
u,v,w	Velocity components, m s^{-1}
V	Volume, m^3
V_w	Wind velocity, m s^{-1}
u_i, u_j	Averaged velocity components, m s^{-1}
u_i', u_j'	Velocity fluctuations, m s^{-1}
$x_i,\ x_j$	Spatial coordinates, m
x,y,z	Cartesian coordinates
y^+	Dimensionless wall coordinate
$-\rho\overline{u_i'u_j'}$	Reynolds stresses, N m^{-2}
∇p	Pressure drop, Pa
Δm	Perforated plate thickness, m

Greek letters

α	Absorber tube absorptivity
α_p	Permeability of the perforated plate, m^2
$\sigma_{h.t}$	Turbulent Prandtl number for energy
β	Plate orientation angle, degrees
δ_{ij}	Kronecker delta
ξ	Emissivity

φ_r	Collector rim angle, degrees
ρ	Density, kg m^{-3}
ρ	Collector Reflectance
λ	Fluid thermal conductivity, Wm^{-1} K^{-1}
η_o	Optical efficiency, %
τ_g	Glass cover transmissivity
τ_w	Wall shear stress
θ	Receiver angle, degrees
μ	Viscosity, Pa s
μ_t	Turbulent viscosity, Pa s
μ_τ	Friction velocity,m/s
μ_{eff}	Effective viscosity, Pa s
v	Kinematic viscosity, m^2 s^{-1}

Subscripts

amb	Ambient state
f	Fluid
gi	Inner glass cover wall
go	outer glass cover wall
i, j, k	General spatial indices
max	Maximum value
o	Reference case (plain absorber tube - no inserts)
ro	Absorber tube outer wall
ri	Absorber tube inner wall
sky	Sky temperature
t	Turbulent
w	Wall

Superscripts

⁻	Mean value
~	Dimensionless value
'	Fluctuation from mean value

1. Introduction

Heat transfer enhancement in heat exchangers and in other thermal applications is of significant importance. Not only does it result in energy savings but has other benefits depending on the application under consideration such as heat exchanger weight and size reduction, reduction in device temperatures and reduction in the temperature difference between process fluids.

In parabolic trough receivers, heat transfer enhancement has potential to reduce absorber tube circumferential temperature gradients [1,2] and also reduce absorber tube temperatures thus lower receiver thermal loss and improved receiver thermal performance [3-5]. Moreover, as

parabolic trough systems with high optical efficiencies and high concentration ratios become feasible [6,7], high heat fluxes and high absorber tube temperature gradients will result. As such, improved heat transfer performance will be essential to minimise absorber tube temperature gradients as well as improve the performance and reliability of the receiver at these high concentration ratios. More still, an increase in concentration ratios leads to increased entropy generation rates due to the increased finite temperature differences as concentration ratios increase [8,9]. As such, heat transfer enhancement can also act to minimise the entropy generation in the receiver. For these reasons, heat transfer enhancement in parabolic trough receivers has received considerable attention in the last few decades.

Passive heat transfer enhancement techniques are widely researched and applied in many industrial applications since they require no direct power input as compared to active techniques. Several researchers have applied some of the passive heat transfer enhancement techniques to improve the performance of parabolic trough receivers. Reddy *et al.* [10] numerically analysed a receiver with various porous and longitudinal fin geometries. Ravi Kumar and Reddy [11] investigated the performance of the receiver with a porous disc. Different angles of orientation, porous disc heights and distances between the consecutive discs were considered. Muñoz and Abánades [2] analysed an internally helically finned absorber tube to improve the thermal performance of the receiver and minimise the temperature gradients in the receiver's absorber tube. Recently Cheng *et al.* [12] analysed the heat transfer enhancement of parabolic trough receivers using unilateral longitudinal vortex generators. In these studies, the potential for improved heat transfer performance in receivers with heat transfer enhancement is demonstrated.

Most heat transfer fluids used in parabolic trough receivers decompose rapidly at temperatures above 400 ^{o}C [13,14], leading hydrogen permeation in the receiver's annulus space which exacerbates receiver heat loss. Therefore, heat transfer enhancement mechanism in the receiver's absorber tube should avoid any hot spots and absorber tube surface modification should be done while taking into account likely thermal stresses. Therefore, use of tube inserts appears to be a sure way of avoiding temperature hotspots and thermal stress in the absorber tube. Porous media or perforated inserts present several benefits when compared with solid inserts such as lightweight, low fluid friction and potential for forcing uniform flow distribution [15]. In this study, the use of perforated plate inserts for heat transfer enhancement in a parabolic trough receiver is investigated.

However, besides improving heat transfer performance, heat transfer enhancement techniques also result in an increase in fluid friction. Therefore, to optimise the performance a particular heat transfer enhancement technique, increasing the heat transfer and reducing fluid friction should be considered at the same time. This presents a multi-objective optimisation problem, in which the heat transfer performance is to be maximised and the fluid friction is to be minimised. In this case, the two objectives are conflicting with each other such that as the heat transfer performance increases the fluid friction also increases. There is no single design that is "best" for all the objectives when both objectives are of the same importance.

In such a case, a set of best solutions often called non-dominated solutions or Pareto optimal solutions [16,17] is sought, such that selecting any one solution in place of another sacrifices quality of one of the objectives while improving the other objective. Genetic algorithms are suited for optimisation of these classes of problems in many applications including fluid flow and heat transfer problems [18]. Detailed description of genetic algorithms and their suitability for use in optimisation of multi-objective problems is provided in Refs. [17,18]. Researchers who have used genetic algorithms for multi-objective optimisation of heat transfer and fluid flow problems include Kim *et al.* [19], Ndao *et al.* [20], Cortes-Quiroz *et al.* [21,22] and Karathanassis *et al.*[23]. Other authors have applied multi-objective optimisation to thermal systems such as refrigeration systems [24] and energy storage systems [25-27].

Most investigations on heat transfer enhancement use the first law of thermodynamics to characterize the resulting thermo-hydraulic performance. Studies that use the second law of thermodynamics to investigate both the thermo-hydraulic and thermodynamic performance of heat transfer enhancement techniques are not wide spread. The second law of thermodynamics provides a means of specifying the quality of the available energy. In this investigation, we use both multi-objective optimisation and thermodynamic optimisation to optimize the heat transfer, fluid friction and thermodynamic performance of a parabolic trough receiver with perforated plate inserts.

2. Physical model and computational domain

The physical model of the receiver with perforated plates under consideration in this study is shown in Figs. 1(a) and 1(b). Similar to the conventional parabolic trough receivers, the space
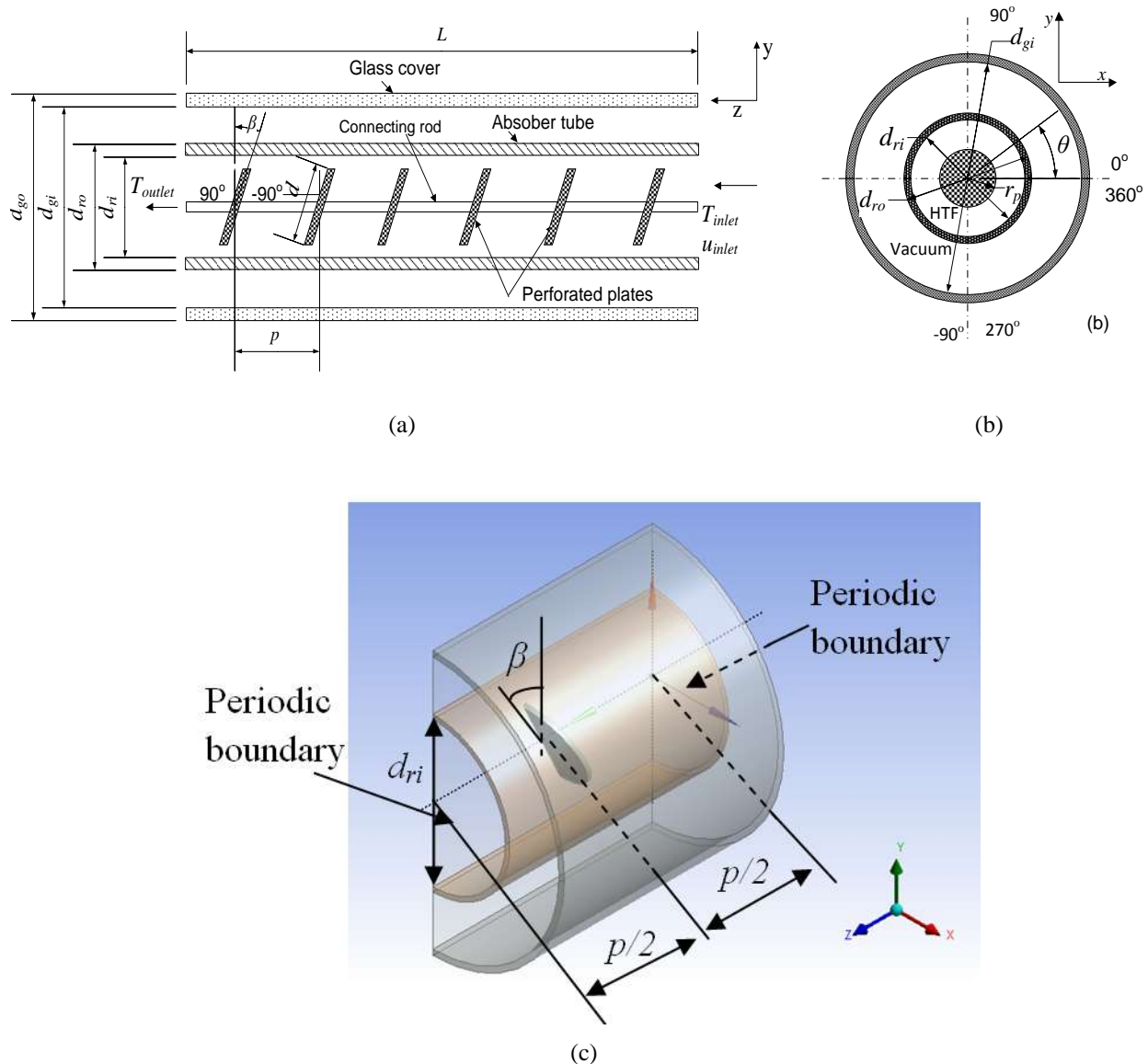
Fig. 1 Representation of the parabolic trough receiver physical model (a) longitudinal section of the receiver with perforated plate inserts (b) cross-section of the receiver tube with perforated plates (c) Periodic computational domain

between the absorber tube and the glass cover is considered evacuated. Thus, only the radiation heat loss takes place between the absorber tube and the glass cover.

From Fig. 1(a), three geometrical parameters of the perforated plate are defined: the spacing between the two consecutive perforated plates (p), the diameter of the perforated plate (d) and the angle of orientation (β). The angle of orientation is measured from the positive y-axis, where β is positive in the anti-clockwise direction and negative in the clockwise direction. In our

analysis, the effect of the central rod and other supports on the receiver's thermal performance is considered negligible.

Because of the symmetrical nature of the problem, only half of the receiver was considered. Furthermore, the flow in the absorber tube becomes periodically fully developed far from the entrance, as such, only a periodic module of the receiver is considered. The computational domain used is shown in Fig. 1(c). The receiver has an absorber tube with an internal diameter of 66 mm and an outer diameter of 70 mm. The glass cover inner and outer diameters are 115 mm and 120 mm respectively similar to the SEGS-LS2 receiver [28]. The geometrical and other parameters used in this study are shown in Table 1.

Table 1. Geometrical and optical values of the parabolic trough collector

Reflector		Receiver		Perforated plate	
a_c	6.0 m	d_{ri}	0.066 m	β	-30° to 30°
L_c	7.8 m	d_{ro}	0.07 m	d	0.03 – 0.06 m
ρ	0.96	τ_g	0.97	p	0.04 – 0.20 m
σ	0.0002 mrad	α	0.96		

3. Numerical analysis

3.1 Governing equations

Due to the high heat fluxes on the receiver's absorber tube, high flow rates are usually used for better heat transfer performance. Therefore, we considered the flow inside the absorber tube to be steady-state and fully developed turbulent. As such, the governing equations are:

Continuity equation

$$\frac{\partial(\rho u_i)}{\partial x_i} = 0 \tag{1}$$

Momentum equation

$$\frac{\partial}{\partial x_j}\left(\rho u_i u_j\right) = -\frac{\partial P}{\partial x_i} + \frac{\partial}{\partial x_j}\left[\mu_{eff}\left(\frac{\partial u_i}{\partial x_j} + \frac{\partial u_j}{\partial x_i}\right) - \frac{2}{3}\mu_{eff}\frac{\partial u_i}{\partial x_i}\delta_{ij} - \rho\overline{u_i' u_j'}\right] + S_m \tag{2}$$

Energy equation

$$\frac{\partial}{\partial x_j}\left(\rho u_j c_p T\right) = \frac{\partial}{\partial x_j}\left(\lambda \frac{\partial T}{\partial x_j} + \frac{\mu_t}{\sigma_{h,t}}\frac{\partial(c_p T)}{\partial x_j}\right) + u_j\frac{\partial P}{\partial x_j} + \left[\mu_{eff}\left(\frac{\partial u_i}{\partial x_j} + \frac{\partial u_j}{\partial x_i}\right) - \frac{2}{3}\mu_{eff}\frac{\partial u_i}{\partial x_i}\delta_{ij} - \rho\overline{u_i' u_j'}\right]\frac{\partial u_i}{\partial x_j} \qquad (3)$$

Where $-\rho\overline{u_i' u_j'}$ are the Reynolds stresses, u_i, u_j are the time-averaged velocity components in the i- and j-directions respectively, T is the time-averaged temperature and P is the time averaged pressure. μ_{eff} is the effective viscosity given by $\mu_{eff} = \mu + \mu_t$ and λ is the fluid thermal conductivity. For relatively low computation cost, the Reynolds stresses are related to the mean velocity gradients using the Boussinesq approach [29] through:

$$-\rho\overline{u_i' u_j'} = \mu_t\left(\frac{\partial u_i}{\partial x_j} + \frac{\partial u_j}{\partial x_i}\right) - \frac{2}{3}\left(\rho k + \mu_t\frac{\partial u_k}{\partial x_k}\right)\delta_{ij} \qquad (4)$$

Where k is the turbulent kinetic energy per unit mass given by

$$k = \frac{1}{2}\left(\overline{u'^2} + \overline{v'^2} + \overline{w'^2}\right) \qquad (5)$$

A number of turbulence models based on the Boussinesq approach have been developed to solve the closure problem in Eqs. (1) - (3). The k-ε models are the widely used and validated models for most flows present in engineering applications [29-31]. For this study, the realisable k-ε model [29,31] was used for turbulence modeling.

The source term (S_m) added to the momentum equation in Eq. (2) represents the pressure drop across the perforated plate. The perforated plate is modeled as porous media of finite thickness with directional permeability over which there is a pressure drop. For porous media, the pressure drop is defined accordingly as a sum of the viscous term and an inertial loss term according to Darcy's law as [29]

$$\nabla p = -\left(\frac{\mu}{\alpha_p}u_i + C_{2p}\frac{1}{2}\rho|u|u_i\right)\Delta m \qquad (6)$$

Where α_p is the permeability of the porous medium, C_{2p} is the inertial resistance factor, Δm is the thickness of the porous media. For perforated plates, the first term representing the viscous loss is negligible and only the inertial loss term should be considered [29,32]. The coefficient C_{2p} has been determined from data presented by Weber *et al.* [33] for perforated plates and flat bar screens. $C_{2p} = 853$ m^{-1} in the stream wise direction for the considered porosity of 0.65 and plate

thickness of 0.0015 m. The values of the inertial resistance factor in other directions are considered very large to restrict flow in those directions.

3.2 Boundary conditions

The boundary conditions used include: (1) a non-uniform heat flux on the outer wall of the absorber tube. The heat flux distribution used in this study is shown in Fig. 2 as determined using
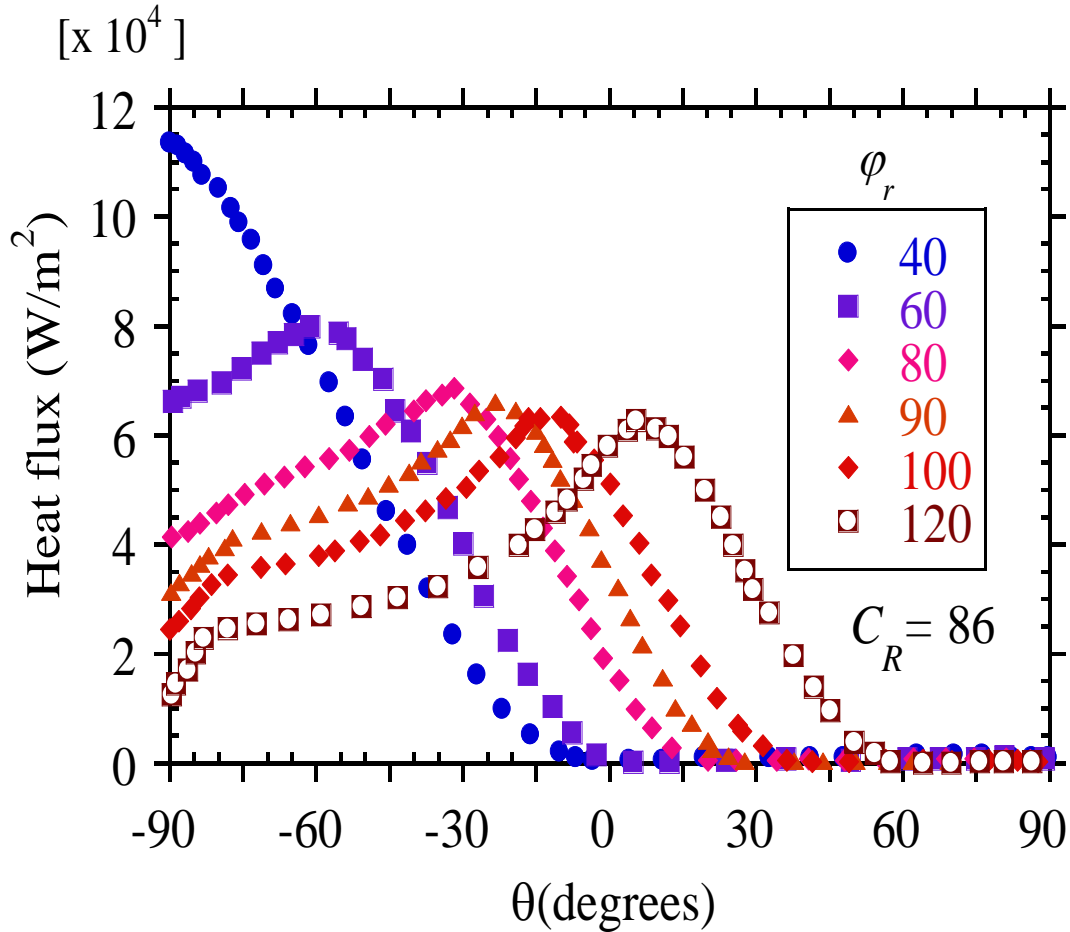

Fig. 2 Heat flux distribution as a function of absorber tube circumferential angle

ray tracing in SolTrace [34]. For this study, the rim angle (φ_r) used was 80° and the aperture width was 6 m giving a geometric concentration ratio (C_R) of 86 slightly higher than the Eurotrough collector $(C_R = 82)$ [1]. The receiver angle θ, is the receiver's circumferential angle shown in Fig. 1(b). The direct normal irradiance (DNI) varies with location, time of the day and tracking mechanism used, in this study a DNI of 1000 W/m^2 which is slightly higher than values

measured by Dudley *et al.*[28] was assumed. (2) Periodic boundary conditions are used for the absorber tube's inlet and outlet. (3) The inner absorber tube walls are considered no-slip and no-penetration. (4) For the inlet and outlet of the receiver's annulus space, symmetry boundary condition is used such that the normal gradients of all flow variables are zero. (5) For the outer wall of the glass cover, a mixed boundary condition is used to account for both radiation and convection heat transfer. The receiver exchanges heat by radiation with the larger enclosure, the sky. The sky temperature is determined as a function of the ambient temperature from García-Valladares and Velázquez [35] as:

$$T_{sky} = 0.0552\, T_{amb}^{1.5} \tag{7}$$

The ambient temperature of 300 K was used and Boltzmann law accounts for this radiation exchange. The convention heat transfer coefficient used for the convection boundary condition is given by Mullick and Nanda [36] as:

$$h_w = V_w^{0.58} d_{go}^{-0.42} \tag{8}$$

Where V_w is the wind speed, taken as 2 m/s in this study and d_{go} is the glass cover outer diameter. The concentration ratio, C_R is defined as $C_R = A_a/A_r$, where A_a is the projected area of the collector's aperture and A_r is the projected area of the absorber tube. (6) On the symmetry plane, the normal velocity and the normal gradients of all flow variables are zero.

3.3 Solution procedure

The numerical solution was implemented was implemented in ANSYS® 14.5. The computational domain was discretised using tetrahedral elements with structured elements in the wall normal directions for the absorber tube and structured hexahedral elements for the receiver's annulus space. The governing equations together with the boundary conditions were solved using a finite-volume method implemented in a computational fluid dynamics code ANSYS FLUENT [29].

The coupling of pressure and velocity and was done with the SIMPLE algorithm [37]. Second-order upwind schemes were employed for integrating the governing equations together with the boundary conditions over the computational domain. To capture the high resolution of gradients in the near wall regions, the y^+ value of about 1 was ensured for all simulations. The enhanced wall treatment [29] was used for modeling the near-wall phenomena for such low values of y^+.

Where $y^+ = y u_\tau / v$, v is the fluid's kinematic viscosity, y is the distance from the wall, and u_τ is the friction velocity given by $u_\tau = \sqrt{(\tau_w / \rho)}$.

The solution was considered converged when the scaled residuals of continuity, momentum, turbulence kinetic energy, turbulent dissipation rate and energy ceased changing after about 100 successive iterations. The values of the scaled residuals after these iterations were in the order of less than 10^{-4} for the continuity equation, less than 10^{-6} for velocity, turbulent kinetic energy and turbulent dissipation rate and less than 10^{-7} for energy.

SYLTHERM 800 was used as the heat transfer fluid [38] in the absorber tube. For fluid temperatures 400 K, 500K and 600 K used the fluid properties are shown in Table 2. The

Table 2. Heat transfer fluid properties [38]

	$T_f = 400$ K	$T_f = 500$ K	$T_f = 600$ K
Density (kg/m^3)	840	746	638
Viscosity (Pa s)	0.002164	0.000816	0.000386
Thermal conductivity (W/m K)	0.1148	0.0958	0.0770
Specific heat capacity (J/kg K)	1791.64	1964.47	2135.30

absorber tube is made of stainless steel (321H) and the glass cover is made of Pyrex® [39]. The emissivity of the absorber tube's selective coating is given by Forristall [39] as

$$\xi = 0.000327(T+273.15) - 0.065971. \tag{9}$$

Where T is the average absorber tube temperature in ^{o}C.

Grid dependence tests were carried out for representative cases of perforated plate arrangements at all Reynolds numbers considered in the study. The solution was considered grid independent when the maximum change of the entropy generation rate, Nusselt number and friction factor was less than 1% as the mesh element size was changed. The number of mesh elements depends on the insert spacing, insert size and insert orientation. In this study, the number of mesh elements were in the range 90 800 – 450 800. The changes in friction factor, Nusselt number and entropy generation as the mesh size was changed are given by

$$\Delta f = \left| \frac{(f^i - f^{i+1})}{f^{i+1}} \right| \le 0.01 \; , \; \Delta Nu = \left| \frac{(Nu^i - Nu^{i+1})}{Nu^{i+1}} \right| \le 0.01 \text{ and } \Delta S_{gen} = \left| \frac{(N_{s,en}^{\;\;i} - N_{s,en}^{\;\;i+1})}{N_{s,en}^{\;\;i+1}} \right| \le 0.01. \tag{10}$$

where $N_{s,en} = S_{gen}/(S_{gen})_o$

The indices i and $i+1$ indicate the mesh before and after refinement respectively. Sample mesh used in this study is shown in Fig. 3.
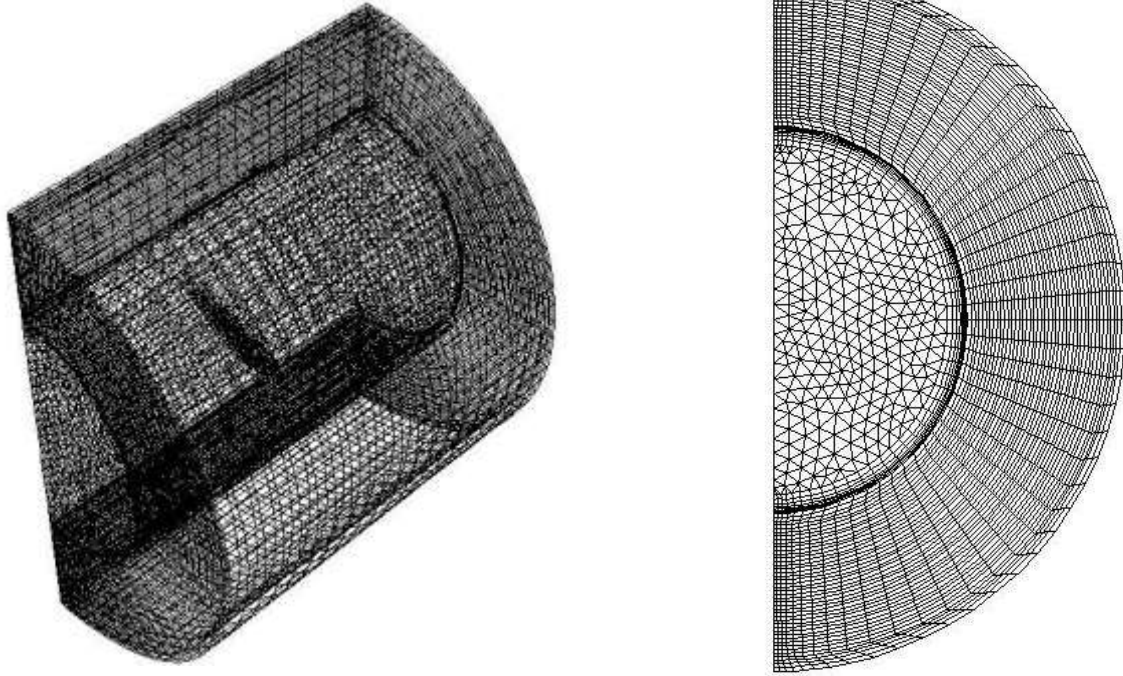
(a) Lateral view   (b) Cross-Section view

Fig. 3 Sample mesh of a receiver with a perforated plate insert

3.4 Data reduction

From Fig. 1(a) the following non-dimensional variables are defined

$$\tilde{p} = p/L; \; \tilde{\beta} = \beta/\beta_{max}; \; \tilde{d} = d/d_{ri} \tag{11}$$

Where L is 1 m and β_{max} *is* 30°, $\tilde{p}$ is the non-dimensional plate spacing, $\tilde{d}$ is the non-dimensional plate size and $\tilde{\beta}$ is the non-dimensional plate orientation angle.

The results from our numerical analysis are presented using the following parameters:

The average heat transfer coefficient is given by

$$h = q'' / (T_{ri} - T_b) \tag{12}$$

In which, T_{ri} is the average inner wall temperature of the absorber tube and T_b is the bulk temperature of the fluid at the periodic boundaries.

The average Nusselt number is given by

$$Nu = h d_{ri} / \lambda \tag{13}$$

Where, λ is the thermal conductivity of the fluid.

The Reynolds number for both the enhanced absorber tube and non-enhanced absorber tube is defined as

$$Re = \frac{u_{inlet} \cdot d_{ri}}{v} \tag{14}$$

Where, v is the kinematic coefficient of viscosity of the heat transfer fluid.

The friction factor is defined as:

$$f = \frac{\Delta P}{\frac{1}{2} \rho \cdot u_{inlet}^2 \cdot \frac{L}{d_{ri}}} \tag{15}$$

4. Optimisation

4.1 Multi-objective optimization

In its general form, a multi-objective optimisation problem can be written as [17]:

Minimise/maximise	$f_m(\mathbf{x})$,	$m = 1, 2, \ldots\ldots\ldots, M$;
Subject to	$g_j(\mathbf{x}) \geq 0$	$j = 1, 2, \ldots\ldots\ldots, J$;
	$h_k(\mathbf{x}) = 0$	$k = 1, 2, \ldots\ldots\ldots, K$;
	$x_i^{(L)} \leq x_i \leq x_i^{(U)}$	$i = 1, 2, \ldots\ldots\ldots, n$.

$$\tag{16}$$

Where $f_m(\mathbf{x})$ is the objective function, M is the number of functions to be optimised. A solution $\mathbf{x}$ is a vector of n decision variables such that $\mathbf{x} = (x_1, x_2, \ldots, x_n)^T$. $g_j(\mathbf{x})$ and $h_k(\mathbf{x})$ are constraint functions with J representing the inequality constraints and K the equality constraints. The last set represents the variable bounds, with each variable taking a value within the specified lower limit $x_i^{(L)}$ and upper limit $x_i^{(U)}$.

Multi-objective optimisation uses the concept of domination, which is implemented in most multi-objective algorithms to obtain a set of solutions that are not dominated [17]. A solution $\mathbf{x}^{(1)}$ is said to dominate solution $\mathbf{x}^{(2)}$ if these two conditions are true [17].

- The solution $\mathbf{x}^{(1)}$ is no worse than $\mathbf{x}^{(2)}$ in all objectives
- The solution $\mathbf{x}^{(1)}$ is strictly better than $\mathbf{x}^{(2)}$ in at least one objective

Determination of a set of solutions that are not dominated with respect to each other is the purpose of multi-objective optimisation. These solutions are often referred to as the non-dominated or Pareto optimal solutions. Given two non-dominated solutions, where both objectives are important, it is not possible to say which of the solutions is better than the other. The solutions in the non-dominated set are better than the rest of the solutions in the design space [17].

4.2 Design variables and objective functions

The three geometrical design variables considered are shown in Fig.1(a), the spacing between two consecutive plates, the orientation angle of the plate and diameter of the perforated plate. The dimensionless form of these variables is $\tilde{p}$, $\tilde{\beta}$ and $\tilde{d}$ respectively as defined in Eq. (11).

The two objective functions to be optimised in this study are the heat transfer performance in terms of the Nusselt number given by Eq. (13) and the pressure drop given in terms of fluid friction given by Eq. (15). The design space for the optimisation process as defined in terms of lower and upper bounds of design variables used was $-1 \leq \tilde{\beta} \leq 1$, $0.31 \leq \tilde{d} \leq 0.91$ and $0.04 \leq \tilde{p} \leq 0.20$.

4.3 Optimisation procedure

The optimisation was carried out using the design exploration toolbox available in ANSYS® 14.5 [16]. The flow chart showing the optimisation procedure is shown in Fig. 4. The optimisation process starts by building an accurate physical model of the problem. This includes selection of design parameters and their ranges of variation as well as specification of performance parameters. An initial solution is then obtained and used as a base case for the optimisation process.
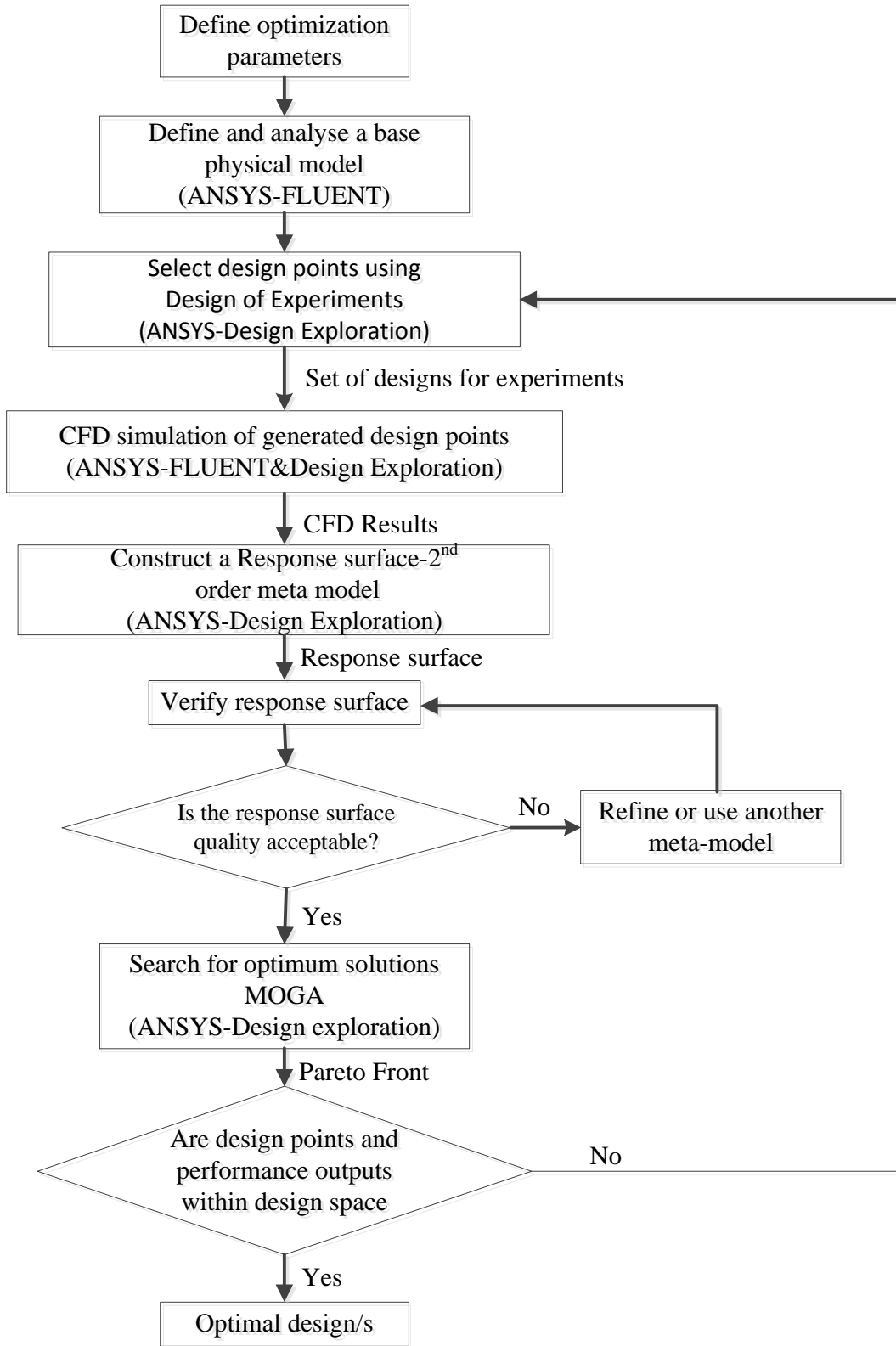
Fig. 4 Multi-objective optimisation flow chart

Using Design of Experiments (DOE), a set of design points corresponding to different geometrical configurations was then generated based on the selected DOE type. For deterministic computer experiments "space filling" designs are considered efficient since they treat the design space equally [16,41]. They also support the use of higher order meta-models including Kriging meta-models adopted for this study [16]. Therefore, the optimal space filling DOE type [16] was used. About 30 design points were sufficient in each case.

Once all the design points are updated, a response surface or a meta-model that relates the performance parameters to the design parameters was constructed. The accuracy of the response surface is essential for the remaining steps [42]. In this study, we used the Kriging meta-model [16] an interpolating meta-modeling technique to improve the accuracy of our response surfaces. The Kriging meta-model in ANSYS® 14.5 [16] has an automated refinement procedure. It determines where more design points are needed in a response surface to improve its accuracy. The refinement terminates when the number of specified refinement points is reached or when the specified predicted relative error has been achieved [16]. The predicted relative error in all cases was set to 5% and 10 refinement points were more than enough for a converged solution.

An optimisation algorithm was then applied to the obtained response surface. The multi-objective genetic algorithm used in ANSYS® 14.5 is a hybrid variant of the famous NSGA-II (Non-dominated sorted genetic algorithm-II) based on controlled elitism concepts [16]. The convergence of the optimisation procedure depends on the problem and the specified Pareto percentage. Convergence was obtained after less than 15 iterations at a given Reynolds number.

The non-dominated or Pareto optimal solutions obtained in the preceding step represent optimal designs in the multi-objective sense. To choose any of them designer needs higher level information such as weights of each objective or relative importance of the objectives. A decision support process which uses a goal-based, weighted, aggregation-based design ranking technique [16] was used to obtain a set number of optimal design candidates. In this method, the design candidates are ranked based on the single weighted objective function. The value of the weighted objective function depends on the weights given to the performance parameters and decision variables according to their order of importance. In this study, all the design parameters and decision variables were assumed equally important. Therefore, default values were used [16].

The purpose of the sensitivity analysis is to investigate the effect of given variables on the objective functions as well as optimal results. In this study, the effect of changing the Reynolds number and inlet temperature on optimal results is investigated. The Reynolds numbers used were in the range $1.04 \times 10^4 \leq Re \leq 1.36 \times 10^6$ depending on the fluid temperature used. The fluid temperatures were fixed at 400 K, 500 K and 600 K in turn at any given flow rate/Reynolds number.

5. Results and discussions

5.1 Validation of numerical results

Our numerical model was validated in a number of steps. First, we have compared our results with experimental data from Dudley *et al.* [28] for temperature gain and collector efficiency to validate that our receiver model is accurate. Good agreement was achieved for both the temperature gain and the collector efficiency with a maximum deviation of less than 8% as shown in Table 3.

Table 3: Temperature gain and collector efficiency validation with experimental data from Dudley *et al.* [28]

	DNI (W/m^2)	Wind speed (m/s)	Air temperature (^{o}C)	Flow rate (L/min)	T_{inlet} (^{o}C)	ΔT (^{o}C) (Experimental)	ΔT (^{o}C) (Present study)	% error ΔT	Efficiency (Experimental)	Efficiency (present study)	% error
1	933.7	2.6	21.2	47.70	102.2	21.80	22.11	1.44	72.51	72.78	0.37
2	968.2	3.7	22.4	47.78	151.0	22.30	22.02	-1.26	70.90	72.11	1.70
3	982.3	2.5	24.3	49.10	197.5	22.00	21.26	-3.36	70.17	70.61	0.63
4	909.5	3.3	26.2	54.70	250.7	18.70	18.90	1.07	70.25	68.20	-2.91
5	937.9	1	28.8	55.50	297.8	19.10	17.71	-7.28	67.98	62.65	-7.85
6	880.6	2.9	27.5	55.60	299.0	18.20	16.95	-6.86	68.92	64.50	-6.41
7	920.9	2.6	29.5	56.80	379.5	18.10	17.39	-3.92	62.34	58.48	-6.19
8	903.2	4.2	31.1	56.30	355.9	18.50	17.22	-6.92	63.83	59.60	-6.63

The perforated plate model was validated using data from Gan and Riffat [43]. The variation of the pressure coefficient $k = p_s/p_v$ with distance from the perforated plate is shown in Fig. 5. The same trend was been obtained in the current work with maximum deviation of less than 3%. (p_s is the static pressure and p_v is the velocity pressure $= \frac{1}{2}\rho v^2$).
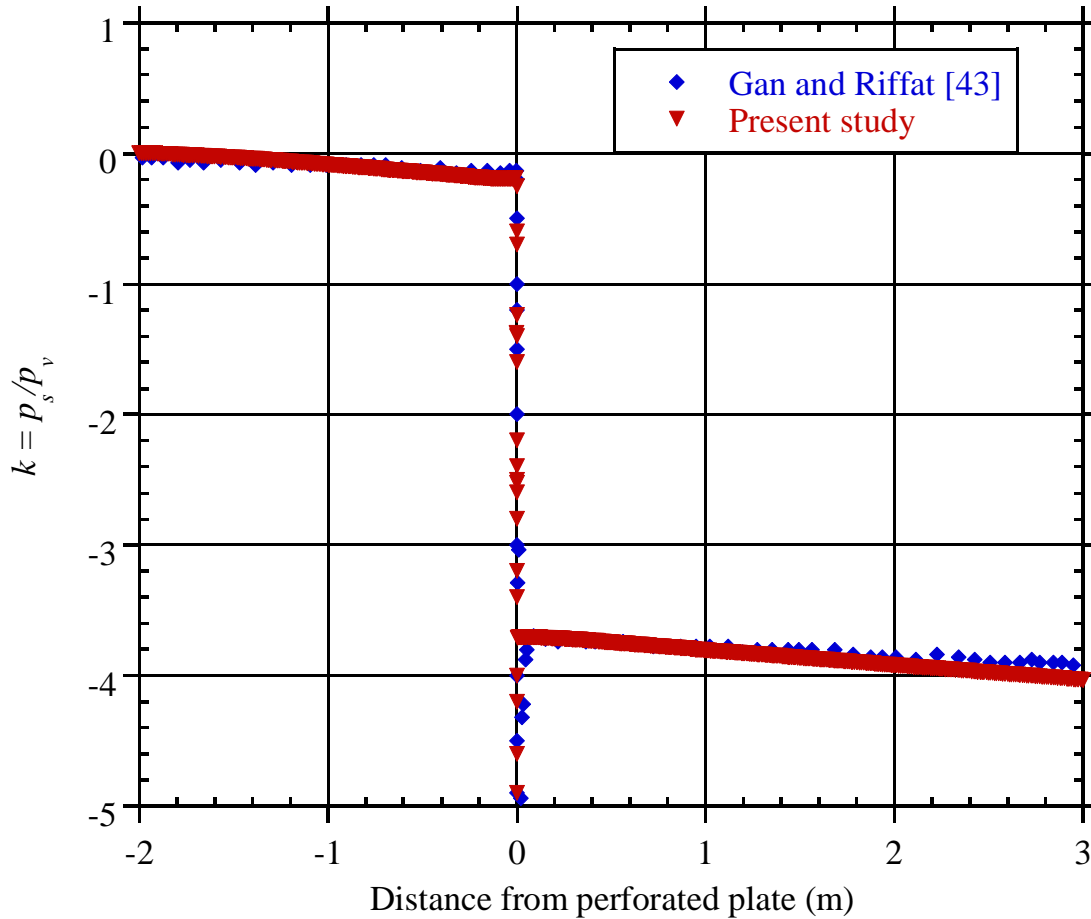
Fig. 5 Validation of the perforate plate model pressure coefficient with literature

Table 4: Validation of the perforated plate model with Ravi Kumar and Reddy [11]

Reynolds number	Nusselt Number			Drag coefficient $= 2\Delta P / \rho u^2$		
	Kumar and Reddy[11]	Present study	Percent Deviation	Kumar and Reddy[3]	Present study	Percent Deviation
6.37×10^4	550	600	9.1	1380	1250	-9.4
1.27×10^5	925	986	6.6	1057	1150	8.8
1.91×10^5	1321	1375	4.1	1008	1040	3.2
2.55×10^5	1704	1750	2.7	982	1000	1.8

Because the perforated plate is modeled in CFD as porous media with negligible viscous loss, numerical data from Ravi Kumar and Reddy [11] for a receiver with a wall mounted porous disc at different angles was also used for further comparison. Table 4 shows the comparison of our

numerical model with Ravi Kumar and Reddy [11] for the orientation of the porous disc of 30°. Good agreement was achieved for both Nusselt number and drag coefficient.

(a)   (b)
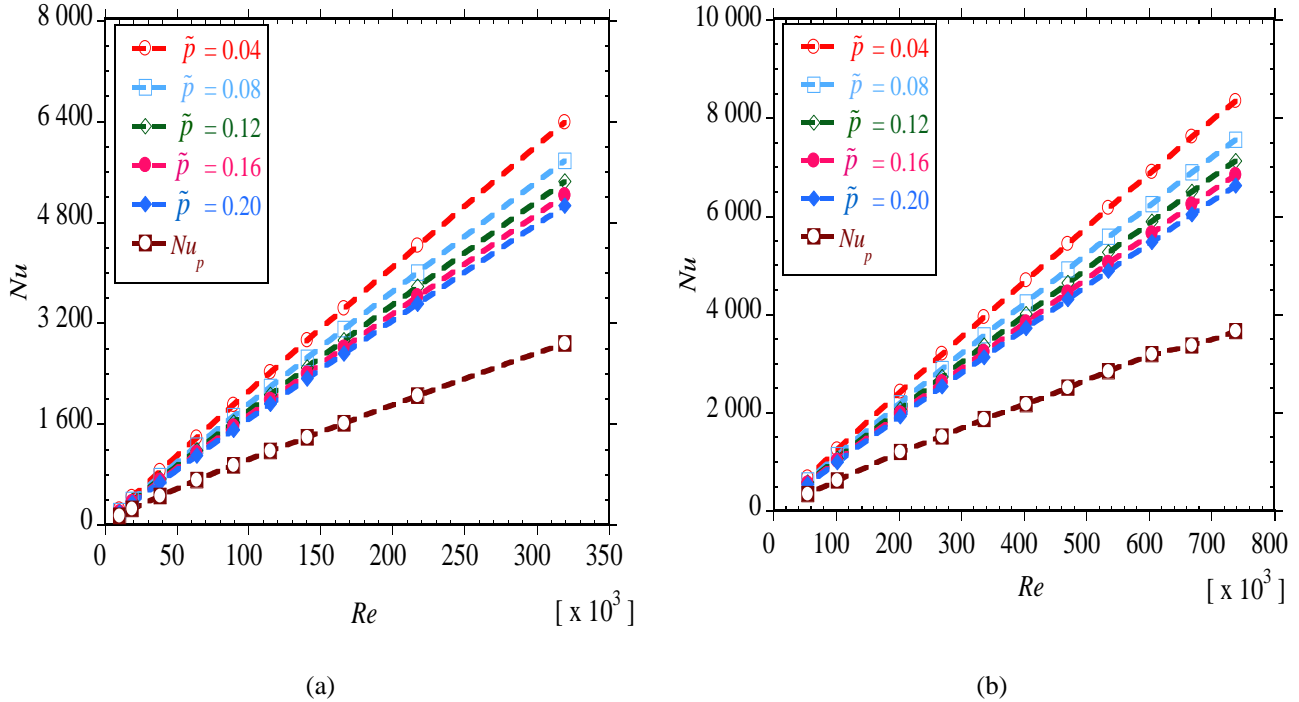
Fig. 6 Variation of Nusselt number with Reynolds number at different values of plate spacing for $\tilde{d} = 0.91$ and $\tilde{\beta} = 1$ at (a) $T_f = 400$ K, (b) $T_f = 650$ K

5.2 Heat transfer and pressure drop variation

Figs. 6(a) and 6(b) show the variation of Nusselt number with Reynolds number at different values of plate spacing for $\tilde{\beta} = 1$ and $\tilde{d} = 0.91$ when the fluid temperature is 400 K and 600 K respectively. As shown, higher values of Reynolds numbers give higher heat transfer rates. The figures further show that, as the spacing between consecutive plates reduces the heat transfer performance increases. Higher Nusselt numbers and Reynolds numbers are observed for a temperature of 600 K than for 400 K at comparable flow rates. This is because as the
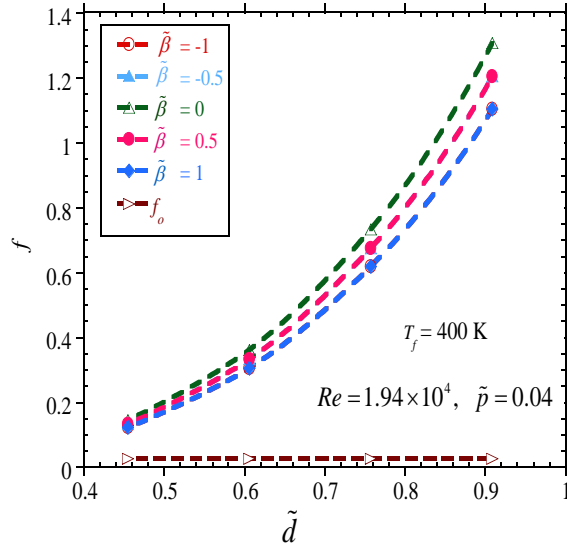
(a)
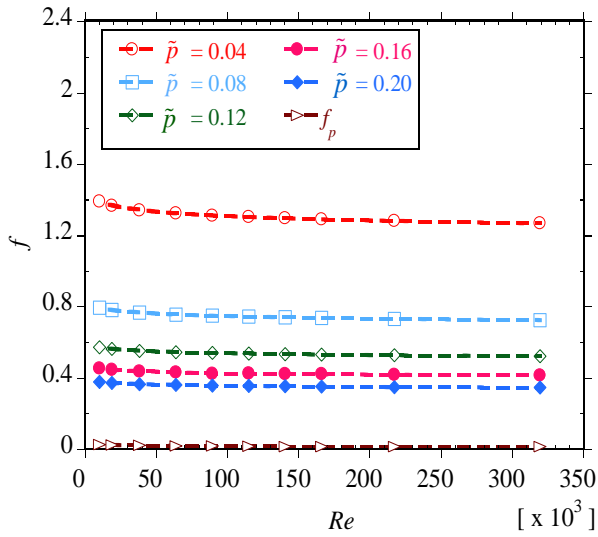
(b)
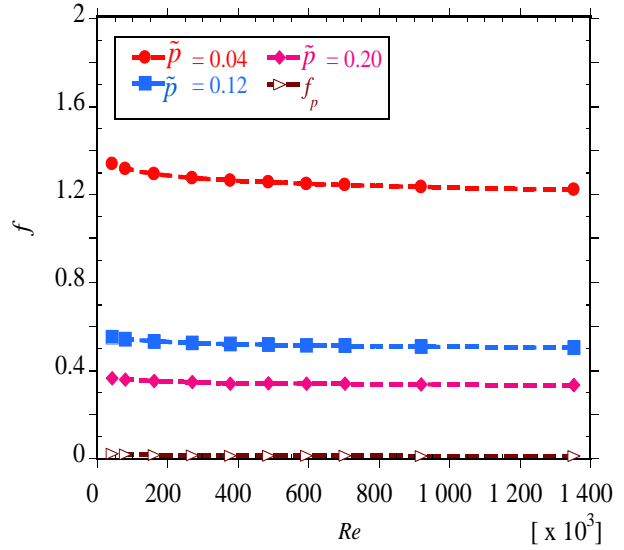
(c)

Fig. 7 Fluid in a receiver with perforated plate inserts (a) as a function of insert size and insert orientation for $Re =$ 1.94 $\times 10^4$, $T_f = 400$ K and $\tilde{p} = 0.04$, (b) as a function of Reynolds number and insert spacing for $\tilde{d} = 0.91$, $\tilde{\beta} = 1$ and $T_f = 400$ K and (c) as a function of Reynolds number and insert spacing for $\tilde{d} = 0.91$, $\tilde{\beta} = 1$ and $T_f = 600$ K

temperatures increase, fluid thermal properties change significantly. The fluid becomes less dense and less viscous giving higher Reynolds numbers, a thinner thermal boundary layer and better heat transfer rates as temperatures increase. As expected, the heat transfer performance

was found to increase as the perforated plate size increases at any given fluid temperature, spacing and Reynolds number. The heat transfer performance also increased as the size of the plate increases and as the orientation angle increases. An increase in plate size leads to higher fluid impingement thus higher heat transfer rates. Positive angles of orientation provide slightly higher fluid impingement on the absorber tube's lower wall, which receives most heat flux (concentrated heat flux). For the range of parameters considered the heat transfer performance increases between 1.02 – 2.34 times compared to a receiver with a plain absorber tube.

Fig. 7 (a) shows the variation of friction factors with plate size at different values of plate orientation angle. Generally, fluid friction increases with plate size. Low fluid friction is shown to exist at both $\tilde{\beta}$ = 1 and $\tilde{\beta}$ = -1. Orienting the plate slightly reduces fluid friction. Equal but opposite angles of orientation are shown to give the same resistance to fluid flow.

Figs. 7 (b) and 7 (c) shows the variation of fluid friction with Reynolds number at different values of plate spacing for T_f = 400 K and 600 K respectively. The same variation is shown to exist at the different temperatures. A decrease in spacing increases fluid friction due to increased flow blockage by the increased number of plates. For the range of parameters considered, fluid friction increases in the range 1.44 – 104 times compared to a receiver with a plain absorber tube.

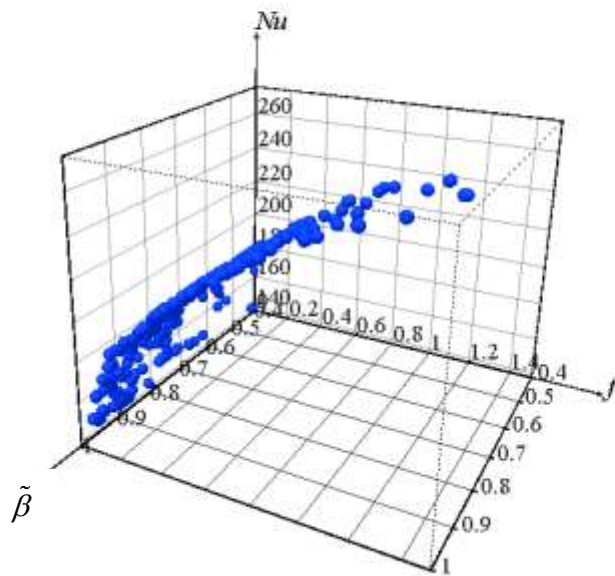## 5.3 Pareto optimal solutions

Fig. 8(a) – 8(c) shows samples of the 3-D Pareto fronts showing the variation of design variables with the objective functions at a Reynolds number of 1.02×10^4 and fluid temperature of 400 K. The figures provide a means for visualising the variation of each variable with the objective functions. A set of solutions from which to choose is shown in these figures. From these figures, a 2-D curve showing the Pareto front for friction factor and Nusselt number is derived as shown in Fig. 8(d). As expected, this is a continuous curve along which selecting any one of the solutions will improve one of the objectives while sacrificing the quality of the other objective. Fig. 9 (a) shows different Pareto optimal solution sets at three different Reynolds numbers and an inlet temperature of 400 K. As discussed earlier, higher Reynolds numbers give better heat transfer performance, thus at high Reynolds numbers the heat transfer performance is higher. Fig. 9 (b) shows the optimal solution sets at a flow rate of 43 m^3/h for different fluid temperatures. The same trend as seen in Figs. 8(d) and 9(a) is obtained. Higher fluid
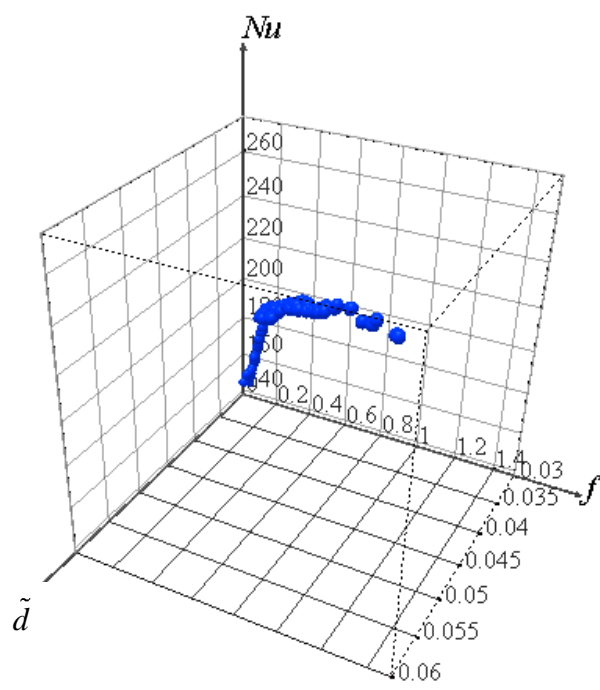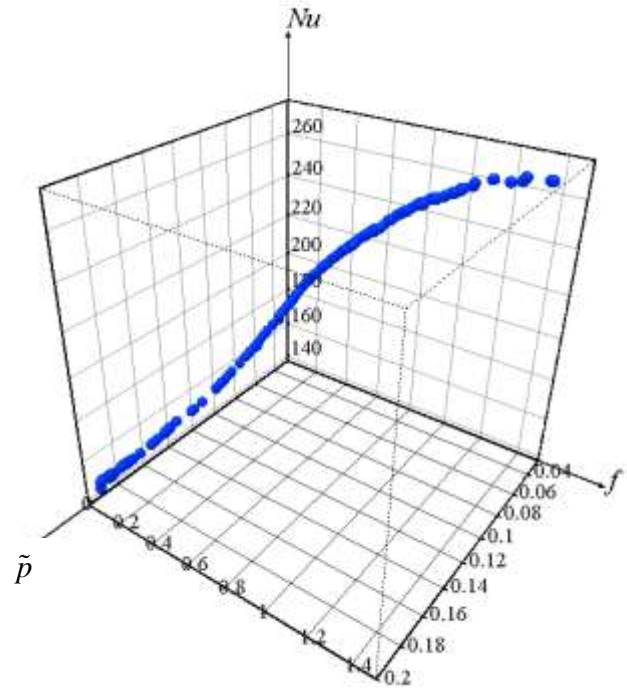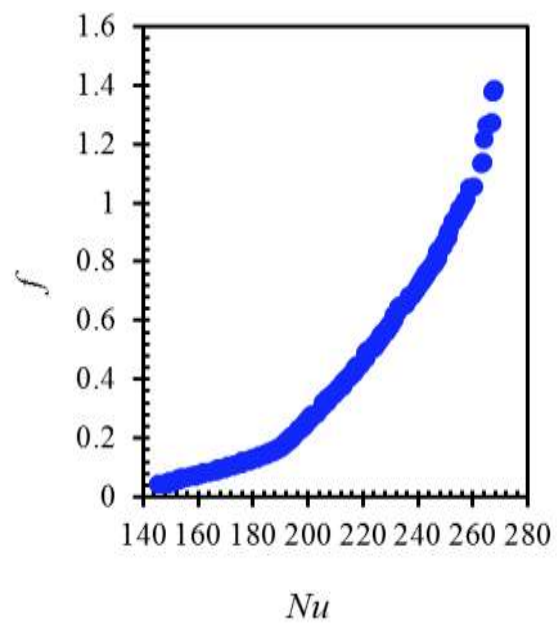
Fig. 8 Pareto optimal solutions at $T_f = 400$ K and Re $= 1.02 \times 10^4$ (a) variation of objective functions with $\tilde{d}$, (b) variation of objective functions with $\tilde{p}$, (c) variation of objective functions with $\tilde{\beta}$ and (d) Pareto front for Nusselt number and friction factor.
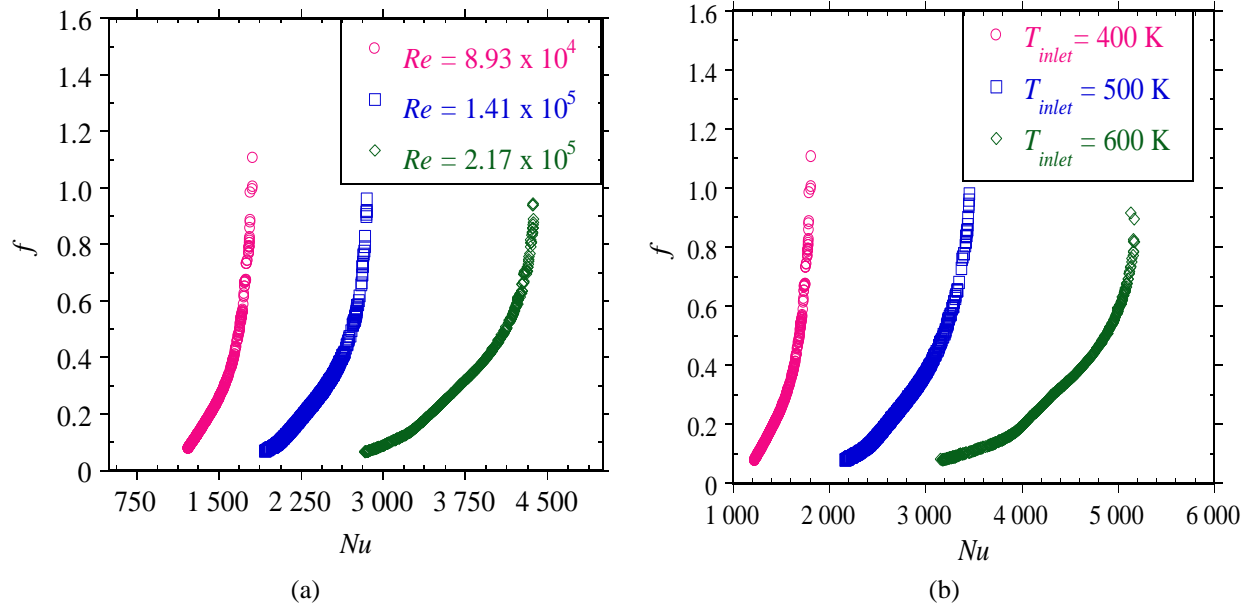
Fig. 9 Pareto front for friction factor and Nusselt number (a) at different Reynolds numbers for a fluid temperature $T_f = 400$ K and (b) at different fluid temperatures for a volume flow rate $\dot{V} = 43 \text{ m}^3/\text{h}$

temperatures show higher Nusselt numbers as was earlier discussed. All the solutions on the Pareto front are optimum solutions for a multi-objective optimisation problem. The choice of the final design point can be obtained, depending on the importance of each objective [16].

Using the decision support process discussed in section 4.3, several design candidates are identified for each value of Reynolds number in their order of importance. Figs. 10 (a-c) show the variation of design variables for the highly ranked design point at each fluid temperature and flow rate. Fig. 10(a) shows the variation of the optimal plate orientation with flow rate at different values of fluid temperature. As shown, the flow rate and fluid temperature do not affect the optimal plate orientation significantly. The value of $\left(\tilde{\beta}\right)_{opt}$ varies between $0.985 - 0.999$ as shown in the figure. Fig. 10(b) shows the variation of the optimal plate size with flow rate at different values of fluid temperature. The optimal plate diameter does not vary significantly with the flow rate. The optimal plate size, $\left(\tilde{d}\right)_{opt}$ is about 0.82, 0.78 and 0.76 at 400 K, 500 K and 600 K respectively. As shown in Fig. 10(c), the optimal plate spacing is very small and almost constant, about 0.036 for lower flow rates, then suddenly increases and becomes constant again
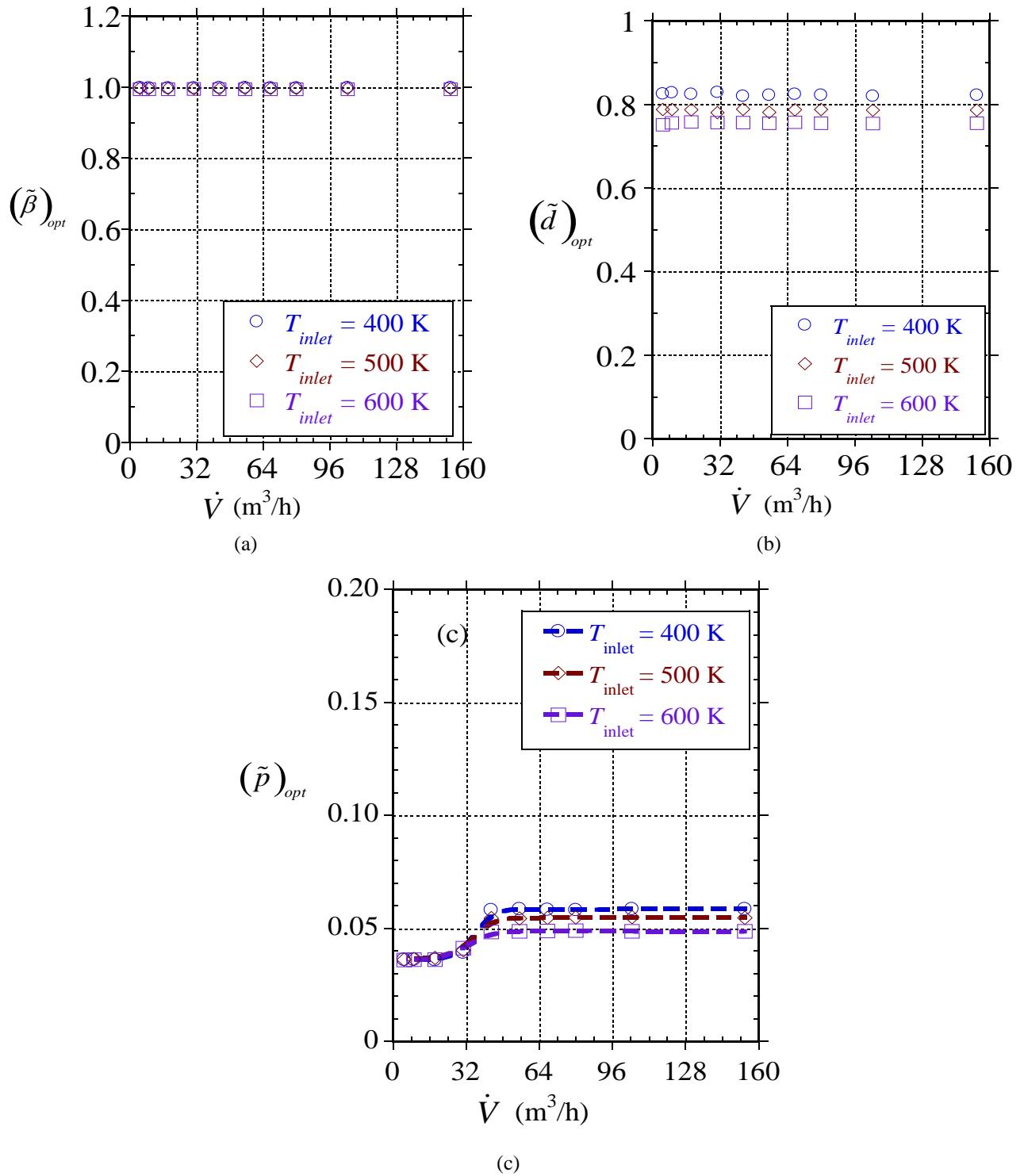
Fig. 10 Variation of optimal design variables with flow rate (a) optimal insert orientation, (b) optimal insert size and (c) optimal insert spacing.

for flow rates higher than 36 m^3/h at each fluid temperature. It should be noted that these values are just representative and will vary depending on the weights for each objective and other constraints as well as the decision support method used.

At the optimal values of plate size, plate spacing and plate orientation in Figs. 10(a-c), the heat transfer performance is enhanced in the range 1.92 – 2.11 while the fluid friction is in the range 30-39 times depending on the flow rate and fluid temperature.

5.4 Thermodynamic optimisation

The entropy generation minimisation method is one of the second law concepts used to define thermodynamically optimal thermal processes, thermal system components and thermal systems. The entropy generation method is widely used for design and optimisation of thermal systems and thermal system components [44-47]. Minimum entropy generation corresponds to the maximum power output since destruction of available work will be a minimum according to the Gouy-Stodola theorem [44].

For heat transfer enhancement, the ratio of entropy generation due to heat transfer enhancement to the entropy generation for a non-enhanced device $N_{s,en}= S_{gen}/(S_{gen})_o$ is used to characterise the thermodynamic performance. This ratio should be less than 1 for better thermodynamic performance [44].

To determine the entropy generation rates, the method proposed by Herwig and Kock [45] was used in this study. The entropy generation rate is determined as a sum of the heat transfer irreversibility $(S_{gen})_H$ and the fluid friction irreversibility $(S_{gen})_F$ from the relevant equations [45]. The validation of this method was done in our previous work [8] and will not be presented here.

Fig. 11(a) shows the variation of the entropy generation due to fluid friction with Reynolds number at different values of plate spacing at $T_f = 400$ K, $\tilde{\beta} = 1$ and $\tilde{d} = 0.91$. Fig. 11 (b) shows the variation of entropy generation due to heat transfer with Reynolds number at different values of plate spacing. In general, as the fluid friction increases, the entropy generation due to fluid friction increases. As the heat transfer performance increases leading to reduction in the finite temperature difference, the entropy generation due to heat transfer irreversibility reduces. The same trend exists at other values of plate orientation and fluid temperatures.
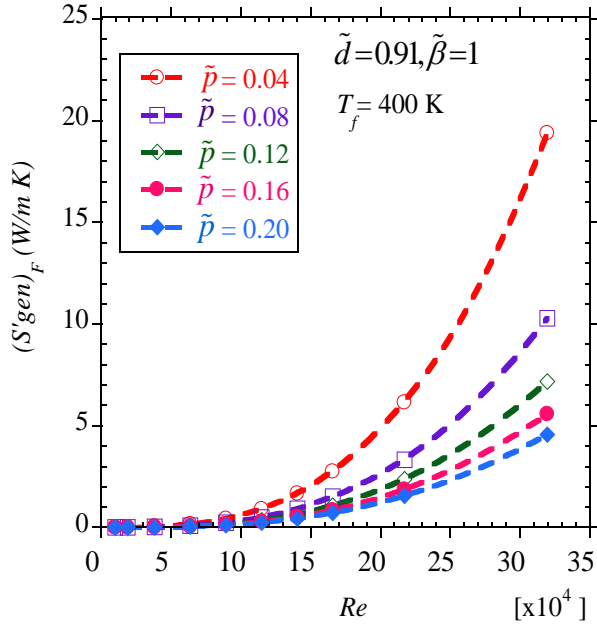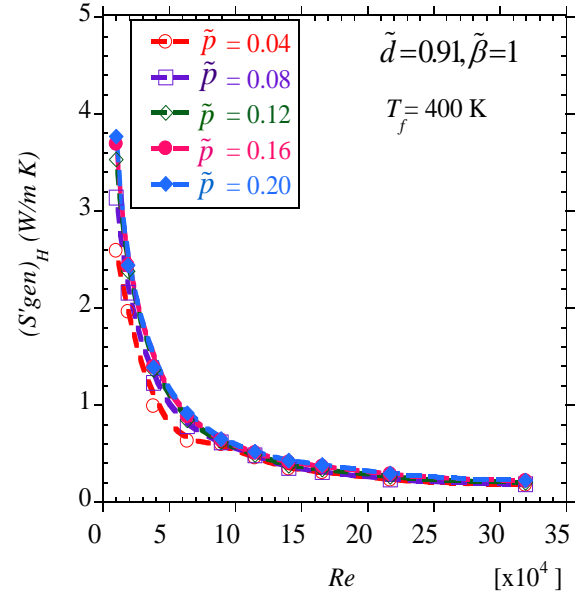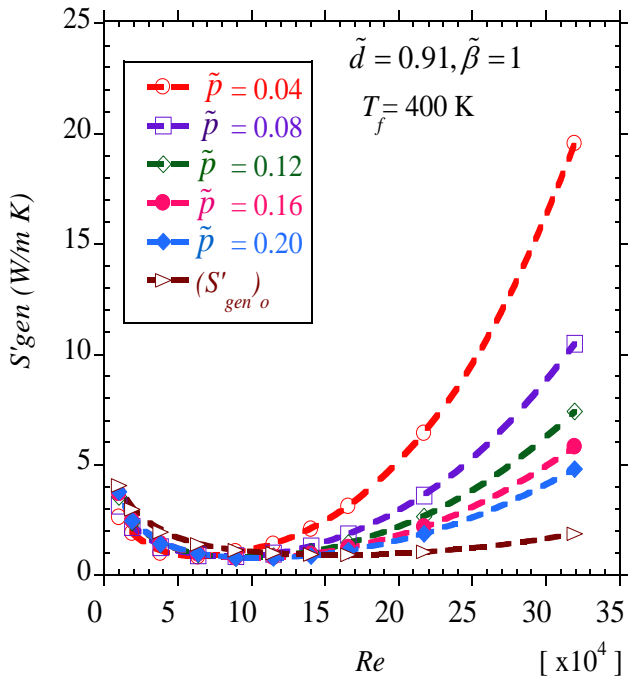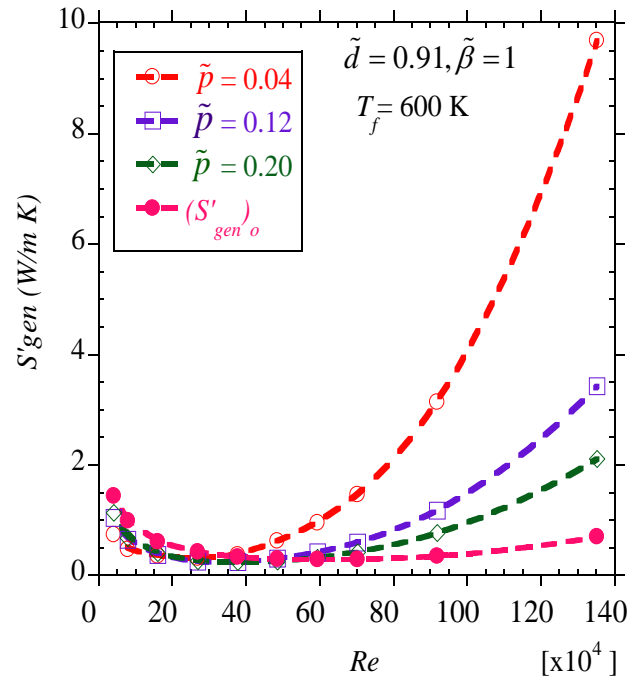
Fig. 11 Variation of entropy generation rate with Reynolds number (a) entropy generation due to fluid friction at $\tilde{d} = 0.91$, $\tilde{\beta} = 1$ and $T_f = 400$ K, (b) entropy generation due to heat transfer at $\tilde{d} = 0.91$, $\tilde{\beta} = 1$ and $T_f = 400$ K, (c) total entropy generation rate at entropy generation due to fluid friction at $\tilde{d} = 0.91$, $\tilde{\beta} = 1$ and $T_f = 400$ K and (d) total entropy generation rate at entropy generation due to fluid friction at $\tilde{d} = 0.91$, $\tilde{\beta} = 1$ and $T_f = 600$ K.

The superposition of Figs. 11(a) and 11 (b) yields the value of the total entropy generation rate as shown in Figs. 11(c) and 11(d) for $\tilde{\beta} = 1$ and $\tilde{d} = 0.91$ at 400 K and 600 K respectively. At all temperatures and a given plate spacing, there is some Reynolds number at which the entropy generation rate is a minimum. Figs. 11(c) and 11 (d) also show that, at low Reynolds numbers the entropy generation due to heat transfer enhancement is less than that in a receiver with a plain absorber tube. At higher Reynolds numbers, the entropy generation rate increases tremendously and becomes more than that in a receiver with plain absorber tube. Lower than the optimal Reynolds numbers, the entropy generation rates are reduced up to 53% depending on the perforated plate geometrical parameters, Reynolds number and fluid temperature.

For the different values of perforated plate orientation, the minimum entropy generation rate occurs at $\tilde{\beta} = 1$. At this value, fluid flow irreversibilities are low due to low fluid friction and heat transfer irreversibilities are high due to higher heat transfer rates. Therefore, optimum values of Reynolds numbers at each value of plate spacing and size are presented for $\tilde{\beta} = 1$. The optimal Reynolds number is determined by fixing the plate spacing and determining the Reynolds number at which the entropy generation is minimum for given sizes of the perforated plate.

Fig. 12 shows the variation of the optimal Reynolds number with insert size at different values of insert spacing. As shown in Figs. 12(a) and 12(b), the optimal Reynolds number generally reduces as the size of the plate increases and increases as plate spacing increases. At low flow rates/Reynolds numbers, larger plate sizes are required for better heat transfer enhancement. At high flow rates, increased turbulence contributes to the improvement in heat transfer and the pressure drop becomes higher such that smaller plate sizes and larger insert spacing are sufficient. Figs. 12(a) and 12(b) also show the optimal Reynolds number to increase as the fluid temperature increases.
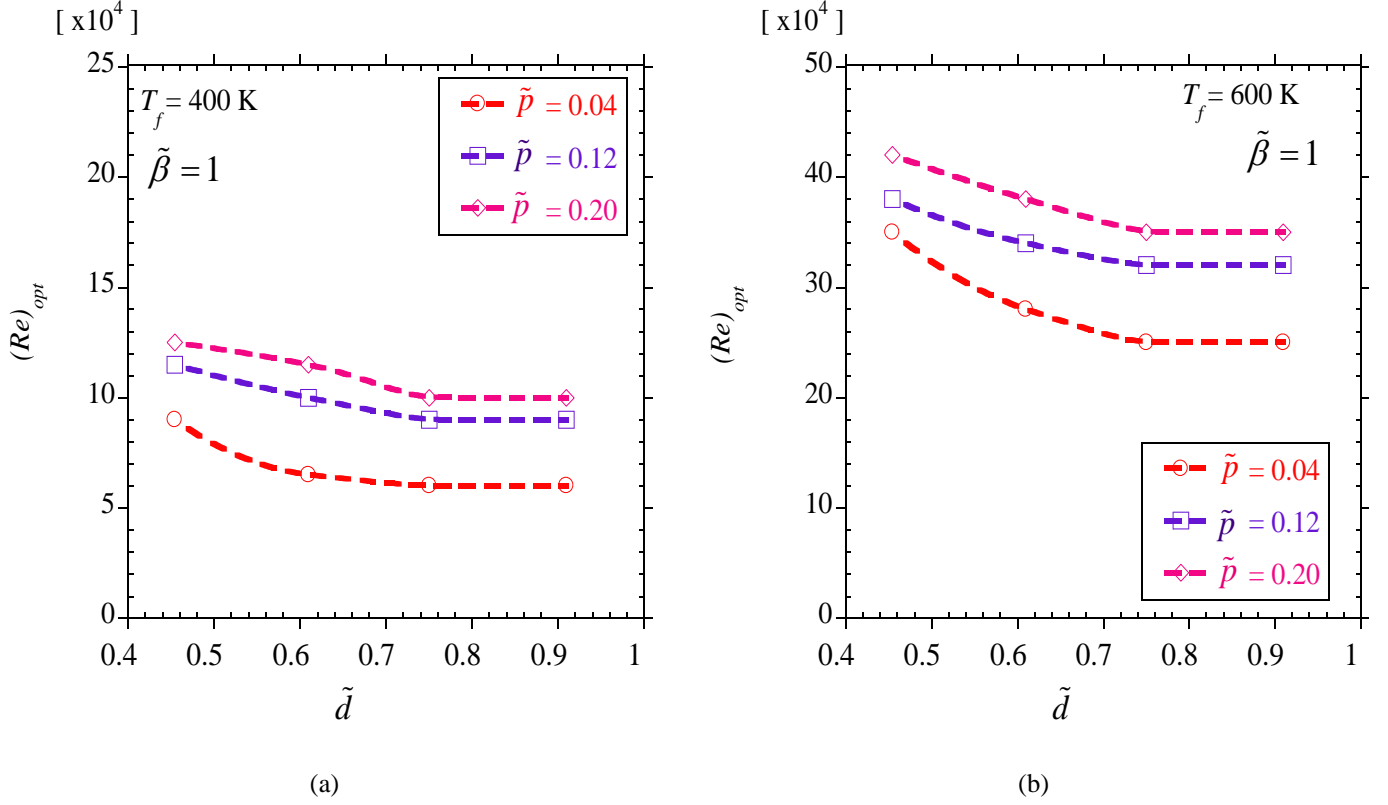
Fig. 12 Variation of the optimal Reynolds number with insert size and insert spacing (a) $\tilde{\beta}=1$ and $T_f = 400$ K and (b) $\tilde{\beta}=1$ and $T_f = 600$ K

6. Conclusion

In the present study, the use of multi-objective optimisation and thermodynamic optimisation in arriving at optimal solutions for a receiver with perforated plate inserts was presented. In the multi-objective optimisation part, the NSGA-II algorithm was used to obtain Pareto optimal solutions for the Nusselt number and pressure drop. Using a goal-based, weighted, aggregation-based decision ranking method, representative design candidates were obtained and presented.

In the thermodynamic optimisation part, the entropy generation minimisation method was used to obtain thermodynamically optimal configurations. At a given Reynolds number, the entropy generation was shown to decrease as the angle of orientation increased. This method also indicated the presence of an optimal Reynolds number for which the generated entropy is a minimum. The optimal Reynolds number was shown to decrease with increasing plate size and

decreasing plate spacing. Below the optimal Reynolds number entropy generation rates are reduced by about 53% with heat transfer enhancement.

7. Acknowledgement

REFERENCES

[1] H. Price, E. Lüpfert, D. Kearney, E. Zarza, G. Cohen, R. Gee, et al., Advances in parabolic trough solar power technology, Journal of Solar Energy Engineering. 124 (2) (2002) 109-125.

[2] J. Muñoz, A. Abánades, Analysis of internal helically finned tubes for parabolic trough design by CFD tools, Applied Energy. 88 (11) (2011) 4139-4149.

[3] Y. He, J. Xiao, Z. Cheng, Y. Tao, A MCRT and FVM coupled simulation method for energy conversion process in parabolic trough solar collector, Renewable Energy. 36 (3) (2011) 976-985.

[4] E. Lüpfert, M. Pfänder, B. Schiricke, M. Eck, Determination of temperature distribution on parabolic trough receivers, 13th International symposium on concentrating solar power and chemical energy technologies. A1-S6 (2006).

[5] F. Burkholder, C. Kutscher, Heat loss testing of Schott's 2008 PTR70 parabolic trough receiver, NREL/TP - 550-45633 (2009) 1-58.

[6] SunShot Initiative-High-concentration low cost parabolic trough system for baseload CSP, available at: http://www1.eere.energy.gov/solar/sunshot/csp_baseload_skyfuel.html. Last accessed [12.02.2013].

[7] A. Schweitzer, W. Schiel, M. Birkle, P. Nava, K.-. Riffelmann, A. Wohlfahrt, et al., ULTIMATE TROUGH® - Fabrication, Erection and Commissioning of the World's Largest Parabolic Trough Collector, Energy Procedia. 49 (0) (2014) 1848-1857.

[8] A. Mwesigye, T. Bello-Ochende, J.P. Meyer, Numerical investigation of entropy generation in a parabolic trough receiver at different concentration ratios, Energy. 53 (0) (2013) 114-127.

[9] A. Mwesigye, T. Bello-Ochende, J.P. Meyer, Minimum entropy generation due to heat transfer and fluid friction in a parabolic trough receiver with non-uniform heat flux at different rim angles and concentration ratios, Energy. 73 (0) (2014) 606-617.

[10] K. Ravi Kumar, K.S. Reddy, Numerical investigation of energy-efficient receiver for solar parabolic trough concentrator, Heat Transfer Engineering. 29 (11) (2008) 961-972.

[11] K. Ravi Kumar, K.S. Reddy, Thermal analysis of solar parabolic trough with porous disc receiver, Applied Energy. 86 (9) (2009) 1804-1812.

[12] Z.D. Cheng, Y.L. He, F.Q. Cui, Numerical study of heat transfer enhancement by unilateral longitudinal vortex generators inside parabolic trough solar receivers, International Journal of Heat and Mass Transfer. 55 (21–22) (2012) 5631-5641.

[13] J. Li, Z. Wang, D. Lei, J. Li, Hydrogen permeation model of parabolic trough receiver tube, Solar Energy. 86 (5) (2012) 1187-1196.

[14] L. Moens, D.M. Blake, Mechanism of hydrogen formation in solar parabolic trough receivers, Journal of Solar Energy Engineering—Transactions of-ASME. 132 (3) (2010) 031006.

[15] Z.F. Huang, A. Nakayama, K. Yang, C. Yang, W. Liu, Enhancing heat transfer in the core flow by using porous medium insert in a tube, International Journal of Heat and Mass Transfer. 53 (5–6) (2010) 1164-1174.

[16] ANSYS® Academic research, release 14.5, ANSYS design exploration user's guide, ANSYS, Inc,.

[17] K. Deb, Multi-objective optimization using evolutionary algorithms, Wiley, New York, 2001.

[18] A. Konak, D.W. Coit, A.E. Smith, Multi-objective optimization using genetic algorithms: A tutorial, Reliability Engineering & System Safety. 91 (9) (2006) 992-1007.

[19] H. Kim, M. Moon, K. Kim, Multi-objective optimization of a cooling channel with staggered elliptic dimples, Energy. 36 (5) (2011) 3419-3428.

[20] S. Ndao, Y. Peles, M.K. Jensen, Multi-objective thermal design optimization and comparative analysis of electronics cooling technologies, International Journal of Heat and Mass Transfer. 52 (19–20) (2009) 4317-4326.

[21] C. Cortes-Quiroz Augusto, M. Zangeneh, A. Goto, On multi-objective optimization of geometry of staggered herringbone micromixer, Microfluidics and Nanofluidics. 7 (1) (2009) 29-43.

[22] C.A. Cortes-Quiroz, A. Azarbadegan, M. Zangeneh, A. Goto, Analysis and multi-criteria design optimization of geometric characteristics of grooved micromixer, Chemical Engineering Journal. 160 (3) (2010) 852-864.

[23] I.K. Karathanassis, E. Papanicolaou, V. Belessiotis, G.C. Bergeles, Multi-objective design optimization of a micro heat sink for Concentrating Photovoltaic/Thermal (CPVT) systems using a genetic algorithm, Applied Thermal Engineering. 59 (1–2) (2013) 733-744.

[24] M. Aminyavari, B. Najafi, A. Shirazi, F. Rinaldi, Exergetic, economic and environmental (3E) analyses, and multi-objective optimization of a CO2/NH3 cascade refrigeration system, Applied Thermal Engineering. 65 (1–2) (2014) 42-50.

[25] A. Shirazi, B. Najafi, M. Aminyavari, F. Rinaldi, R.A. Taylor, Thermal–economic–environmental analysis and multi-objective optimization of an ice thermal energy storage system for gas turbine cycle inlet air cooling, Energy. 69 (0) (2014) 212-226.

[26] M. Navidbakhsh, A. Shirazi, S. Sanaye, Four E analysis and multi-objective optimization of an ice storage system incorporating PCM as the partial cold storage for air-conditioning applications, Applied Thermal Engineering. 58 (1–2) (2013) 30-41.

[27] S. Sanaye, A. Shirazi, Four E analysis and multi-objective optimization of an ice thermal energy storage for air-conditioning applications, International Journal of Refrigeration. 36 (3) (2013) 828-841.

[28] E.V. Dudley, J.G. Kolb, A.R. Mahoney, T. Mancini R., M. Sloan, D. Kearney, Test results: SEGS LS-2 solar collector, SAND94-1884 (9/28/2012) (1994).

[29] ANSYS® Academic research, release 14.5, ANSYS FLUENT, theory guide, ANSYS, Inc,.

[30] H.K. Versteeg, W. Malalasekera, An introduction to computational fluid dynamics: the finite volume method,Pearson/Prentice Hall, Harlow, England, 2007.

[31] T. Shih, W.W. Liou, A. Shabbir, Z. Yang, J. Zhu, A new k-ϵ eddy viscosity model for high reynolds number turbulent flows, Computers & Fluids. 24 (3) (1995) 227-238.

[32] S.M.E. Haque, M.G. Rasul, M.M.K. Khan, A.V. Deev, N. Subaschandar, Numerical modelling for optimizing flow distribution inside an electrostatic precipitator, International Journal of Mathematics and Computers in simulation. 1 (2007) 255-261.

[33] L.J. Weber, M.P. Cherian, M.E. Allen, M. Muste, Headloss characteristics for perforated plates and flat bar screens, 411 (March, 2000) 1-95.

[34] NREL, SolTrace optical modelling software, 2012.7.9 (2012).

[35] O. García-Valladares, N. Velázquez, Numerical simulation of parabolic trough solar collector: Improvement using counter flow concentric circular heat exchangers, International Journal of Heat and Mass Transfer. 52 (3–4) (2009) 597-609.

[36] S.C. Mullick, S.K. Nanda, An improved technique for computing the heat loss factor of a tubular absorber, Solar Energy. 42 (1) (1989) 1-7.

[37] S.V. Patankar, D.B. Spalding, A calculation procedure for heat, mass and momentum transfer in three-dimensional parabolic flows, International Journal of Heat and Mass Transfer. 15 (10) (1972) 1787-1806.

[38] SYLTHERM 800 heat transfer fluid:product techinical data, http://www.dow.com/heattrans/products/synthetic/syltherm.htm. Last accessed [14.02.2014].

[39] R. Forristall, Heat transfer analysis and modeling of a parabolic trough solar receiver implemented in Engineering Equation solver, NREL/TP-550-34169 (October 2003) 1-145.

[40] Y.A. Çengel, A.J. Ghajar, Heat and mass transfer: fundamentals & applications,McGraw-Hill, New York, 2011.

[41] T.W. Simpson, J.D. Poplinski, P.N. Koch, J.K.Allen, Metamodels for computer-based engineering design: survey and recommendations, Engineering with computers. 17 (2) (2001) 129-150.

[42] R. Myers H., D.C. Montgomery, Response surface methodology: process and product optimization using designed experiments, John Wiley and Sons,Inc, Canada, 2002.

[43] G. Gan, S.B. Riffat, Pressure loss characteristics of orifice and perforated plates, Experimental Thermal and Fluid Science. 14 (2) (1997) 160-165.

[44] A. Bejan, Entropy generation minimization: the method of thermodynamic optimization of finite-size systems and finite-time processes, CRC Press, Boca Raton, Fla., 1996.

[45] F. Kock, H. Herwig, Entropy production calculation for turbulent shear flows and their implementation in cfd codes, International Journal of Heat and Fluid Flow. 26 (4) (2005) 672-680.

[46] W.G. le Roux, T. Bello-Ochende, J.P. Meyer, Thermodynamic optimisation of the integrated design of a small-scale solar thermal Brayton cycle, International Journal of Energy Research. 36 (11) (2012) 1088-1104.

[47] J. Baloyi, T. Bello-Ochende, J.P. Meyer, Thermodynamic optimisation and computational analysis of irreversibilities in a small-scale wood-fired circulating fluidised bed adiabatic combustor, Energy. 70 (0) (2014) 653-663.